Chemical Shift Mapped DNA-Binding Sites and ^{15}N Relaxation Analysis of the C-Terminal KH Domain of Heterogeneous Nuclear Ribonucleoprotein K

James L. Baber,[‡] David Levens,[§] Daniel Libutti,[§] and Nico Tjandra*,[‡]

Laboratory of Biophysical Chemistry, Building 3, National Heart, Lung, and Blood Institute, National Institutes of Health, Bethesda, Maryland 20892-0380, and Laboratory of Pathology, National Cancer Institute, National Institutes of Health, Bethesda, Maryland 20892

Received January 19, 2000; Revised Manuscript Received March 13, 2000

ABSTRACT: The K homology (KH) motif is one of the major classes of nucleic acid binding proteins. Some members of this family have been shown to interact with DNA while others have RNA targets. There have been no reports containing direct experimental evidence regarding the nature of KH module−DNA interaction. In this study, the interaction of the C-terminal KH domain of heterogeneous nuclear ribonucleoprotein K (KH3) with it's cognate single-stranded DNA (ssDNA) are investigated. Chemical shift perturbation mapping indicates that the first two helices, the conserved GxxG loop, β1, and β2, are the primary regions involved in DNA binding for KH3. The nature of the KH3−ssDNA interaction is further illuminated by a comparison of backbone ^{15}N relaxation data for the bound and unbound KH3. Relaxation data are also used to confirm that the backbone of wild-type KH3 is structurally identical to that of the G26R mutant KH3, which was previously published. Amide proton exchange experiments indicate that the two helices involved in DNA binding are less stable than other regions of secondary structure and that a large portion of KH3 backbone amide hydrogens are protected in some manner upon ssDNA binding. The major backbone dynamics features of KH3 are similar to those of the structurally comparable human papillomavirus-31 E2 DNA binding domain. Secondary structure information for ssDNA-bound wild-type KH3 is also presented and shows that binding results in no global changes in the protein fold.

hnRNP K[1] is a transcription factor for the human c-*myc* proto-oncogene (*1*, *2*). It specifically binds and transactivates the CT element, a positive-acting cis-element 100−150 bp upstream of the c-*myc* P1 promoter. The CT element contains five slightly imperfect CT repeats (CCCTCCCCA) and is single stranded (ss) in the hnRNP K-bound form (*3*, *4*). The mechanism by which hnRNP K promotes c-*myc* transcription has not been elucidated. Concurrently, there is evidence that hnRNP K interacts with other proteins, including the TATA-binding protein (TBP) (*1*), that affect transcription (*5*). Indeed, one cannot presently exclude the idea that hnRNP K may have multiple functions in it's role as a c-*myc* transcription enhancer. Bomstyk et al. (*5*) and Ostareck-Lederer et al. (*6*) have published reviews that summarize a variety of additional molecular partners for hnRNP K, which include proteins involved in signal transduction and gene regulation. More recently, hnRNP K was shown to interact with herpes simplex IE63 protein (*7*), hepatitis C core protein (*8*), and transcription factor C/EBPβ (*9*). hnRNP K also mediates translation of human papillomavirus-16 L2 capsid protein (*10*) and erythroid 15-lipoxygenase (*11*) mRNAs. Additionally, the activities of Sp1 and Sp3 transcription factors for a neuronal nicotinic acetylcholine receptor were shown to be affected by the presence of hnRNP K (*12*).

Previous work demonstrated that hnRNP K homology (KH) domains are responsible for the sequence-specific ssDNA-binding affinity of hnRNP K (*4*). KH modules are approximately 70 residues in length and possess a highly conserved hydrophobic core (*13*, *14*). The two N-terminal KH domains (KH1 and KH2) of hnRNP K are separated by only ∼35 residues, whereas the sequential separation between KH2 and a third C-terminal KH domain (KH3) is much larger (∼175 residues). Other proteins possessing a similar asymmetric sequential arrangement of three KH modules as noted by Lewis et al. (*15*) include hnRNP's E1 and E2, Nova-1, Nova-2, and Ybr232c. Tomonaga and Levens (*4*) showed that two nonoverlapping hnRNP K fragments, one containing KH1 and KH2 and the other encompassing KH3, are each sufficient for sequence-specific binding to the single-stranded CT element. This study also showed that the same fragments bound RNA analogs of CT repeats, but with lesser affinity.

Despite evidence that, in addition to hnRNP K, other KH-containing proteins such as FBP bind DNA (*16*), the KH domain is generally regarded as a RNA-binding motif in the literature (*17*). Sam68 and FMR1 bind both DNA and RNA

* To whom correspondence should be addressed. Phone: (301) 402-3029. Fax: (301) 402-3405. E-mail, nico@helix.nih.gov.

[‡] Laboratory of Biophysical Chemistry.

[§] Laboratory of Pathology.

[1] Abbreviations: hnRNP, heterogeneous nuclear ribonucleoprotein; KH, K homology; KH3, C-terminal KH domain of hnRNP K; CT15, 5′-TTC CCC TCC CCA TTT-3′ oligonucleotide; mutKH3, G26R mutant of KH3; wtKH3, wild-type KH3; KH3−CT15, wtKH3−CT15 complex; ss, single-stranded; ds, double-stranded; DBD, DNA-binding domain; aa, amino acid; NOE, nuclear Overhauser effect; NOESY, nuclear Overhauser enhancement spectroscopy; NMR, nuclear magnetic resonance; HSQC, heteronuclear single quantum correlation; RMS, root-mean-square; BPV, bovine papillomavirus; HPV, human papillomavirus.

10.1021/bi000105e
Published on Web 04/27/2000

(*18*). A single mutation in one of the KH domains of FMR1 abolishes RNA binding (*19*) and is associated with fragile X mental retardation syndrome (*20*). However, a specific in vivo nucleic acid target for FMR1 has not been identified. hnRNP K, as the name implies, was initially discovered as a component of hnRNP complexes and thus presumed to play a role in the transport and/or processing of RNA. hnRNP K and a hnRNP K fragment encompassing KH3 each bind a synthetic RNA homopolymer [poly(rC)] in vitro, but no specific in vivo RNA target has been identified. Pyrimidine-rich untranslated regions of some RNAs were posited as likely candidates (*21*, *22*). Given the reported affinity of hnRNP K for various proteins (*5*), one cannot exclude the possibility that its presence in hnRNP complexes is due to protein−protein interaction. While a number of reports address KH−RNA interactions (*19*, *23*−*27*), this fact alone does not dispute the evidence or preclude the notion that KH domains can also bind DNA. Dejgaard and Leffers (*13*) suggested it is likely that, for proteins with multiple KH motifs, KH domain cooperativity was necessary for nucleic acid binding in some cases whereas a single KH domain was sufficient for binding in others. Therefore, one cannot even presently discount the idea that some KH modules of a given protein bind DNA whereas others in the same protein interact with RNA.

We recently reported the solution structure of the G26R mutant of the C-terminal KH (mutKH3) module of hnRNP K to begin revealing the nature of the molecular mechanisms of the multifunctional hnRNP K protein (*28*). Structures of KH6 of vigilin (*14*), KH1 of FMR1 (*29*), and the KH3 domains of Nova-1 and Nova-2 (*15*) have also been reported to date. The KH module is a three-stranded antiparallel β-sheet covered by three (or two) α-helices in all cases. We noted that these structures are similar to the bovine papillomavirus (BPV) E2 (*30*) and Epstein−Barr nuclear antigen 1 (EBNA1) (*31*, *32*) DNA-binding domains. Furthermore, the distribution of basic residues in the binding region of BPV E2 was remarkably similar to that of the binding region predicted for KH3 of hnRNP K (*28*).

In this paper, we report the chemical shift mapped ssDNA-binding regions of wild-type KH3 (wtKH3). Identification of wtKH3's binding region is crucial as there is currently much speculation regarding this issue. The oligonucleotide selected for this study is comprised of one CT repeat flanked with three nucleotides on each end (CT15). Gel assays show that oligonucleotides containing multiple CT repeats bind KH3 better than the single repeat used in this study (*4*). However, the single CT repeat was chosen so as to minimize the possibility of multiple binding sites. The results of a titration are presented and provide an estimate of the affinity of wtKH3 for CT15. Much of this paper is devoted to backbone ^{15}N relaxation data for mutKH3, wtKH3, and KH3−CT15 as well as the analysis of these data. This relaxation data provides additional insight into the nature of the KH3−CT15 interaction.

MATERIALS AND METHODS

Samples. The KH3 modules used in this study span the last 85 C-terminal residues of hnRNP K (residues 379−463). Both wt- and mutKH3 were expressed as fusion proteins with glutathione-S-transferase and resulted in the net addition of four residues to the N-terminus of each KH3 domain. Expression and purification procedures for wtKH3 were analogous to those described for mutKH3 (*28*). CT15 (5′-TTC CCC TCC CCA TTT-3′) was purchased from The Midland Certified Reagent Company (Midland, TX).

General NMR Spectroscopy. All NMR experiments were performed on a Bruker DMX600 equipped with a shielded *x*, *y*, *z*-pulsed field gradient triple resonance 5 mm probehead. NMRPipe (*33*) and PIPP/STAPP (*34*) software were used to process and analyze, respectively, all spectra. The ^{15}N-^{13}C labeled KH3−CT15 sample used in the heteronuclear assignment and NOESY experiments contained 1.0 mM wtKH3 (uniformly ^{15}N-^{13}C labeled), 1.2 mM CT15, 14 mM KCl, 4.2 mM NaCl, 0.048 mM KH_2PO_4, 0.14 mM Na_2HPO_4, 0.04% NaN_3, and 10% D_2O at a pH* of 5.5. 3D ^{15}N separated NOESY experiments with mixing times of 150, 150, and 100 ms for mutK3, wtKH3, and KH3−CT15, respectively, aided in backbone assignments and identification of secondary structure. Sample conditions for each ^{15}N sample are listed below.

KH3−CT15 Titration. The wtKH3 NMR sample used for the CT15 titration initially contained 0.46 mM wtKH3 (uniformly ^{15}N labeled), 25 mM KCl, 6.8 mM NaCl, 0.076 mM KH_2PO_4, 0.23 mM Na_2HPO_4, 2.3 mM NaN_3, and 6.2% D_2O at a pH* of 5.5. At the end of the titration, the NMR sample contained 0.38 mM wtKH3, 0.48 mM CT15, 25 mM KCl, 6.8 mM NaCl, 0.076 mM KH_2PO_4, 0.23 mM Na_2HPO_4, 2.3 mM NaN_3, and 6.8% D_2O. The CT15 solution used for the titration contained 2.8 mM CT15, 24 mM KCl, 7.0 mM NaCl, 0.078 mM KH_2PO_4, 0.23 mM Na_2HPO_4, 2.3 mM NaN_3, and 9.6% D_2O at a pH* of 5.5. The titration was performed by sequentially adding 4, 4, 8, 10, 13, 13, and 20 μL aliquots of the 2.8 mM CT15 solution to 350 μL of the 0.46 mM wtKH3 NMR sample. The progress of the titration was monitored by ^{1}H-^{15}N HSQC spectra acquired at 33 °C on the Bruker DMX600.

Backbone ^{15}N Relaxation Measurements. The following three samples were used for ^{15}N relaxation measurements: (1) 0.64 mM wtKH3 (uniformly ^{15}N labeled), 0.09% NaN_3, 3 mM NaCl, and 10% D_2O at a pH* of 4.0; (2) 0.64 mM mutKH3 (uniformly ^{15}N labeled), 0.06% NaN_3, 3 mM NaCl, and 10% D_2O at a pH* of 4.0; (3) 0.65 mM wtKH3 (uniformly ^{15}N labeled), 0.70 mM CT15, 0.07% NaN_3, 1 mM KCl, and 9.3% D_2O at a pH* of 5.5. Experiments were performed at 27 °C for the unbound wtKH3 and mutKH3 and at 33 °C for the KH3−CT15 complex. All data sets consisted of 128* × 512* complex data points which were zero-filled to 512 × 2048 data points. The ^{1}H carrier was positioned at the water frequency and the ^{15}N carrier was at 116.5 ppm for all experiments. States-TPPI quadrature detection in t_1 (*35*) was implemented in all cases. All experiments were performed twice to calculate the pairwise root-mean-square (pw-rms) difference. Average errors reported in this study are half of their respective pw-rms values.

^{15}N T_1 and $T_{1\rho}$ pulse sequences were modified from those reported by Barbato et al. (*36*) to include the Watergate scheme (*37*), pulsed field gradient (*38*), and a semiconstant time evolution period in t_1 (*39*). The $T_{1\rho}$ experiment utilized continuous ^{15}N spin-locking (*40*) with a 2.5 kHz radio frequency field for the mutKH3 and wtKH3 samples and a 2.1 kHz field for the KH3−CT15 sample. The following ^{15}N relaxation delays were used for the T_1 measurements: 8, 88,

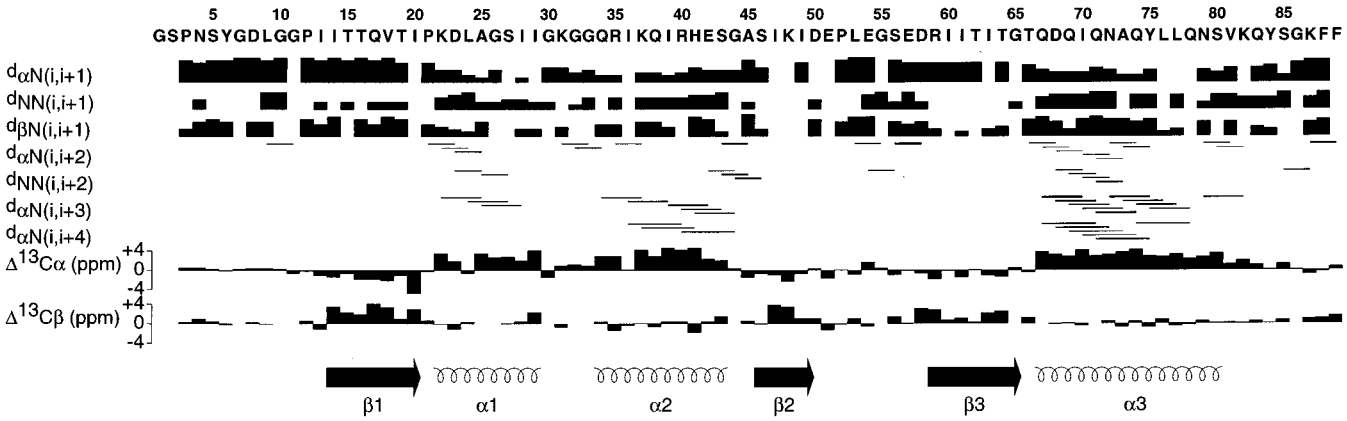

FIGURE 1: Summary of sequential and medium-range NOEs and ^{13}C secondary chemical shifts for wtKH3 bound to CT15 (KH3−CT15). Secondary structural elements of mutKH3 are shown at the bottom.

192, 392, 560, 784, 976, and 1200 ms for wt- and mutKH3; 8, 88, 256, 504, 728, 976, 1120, and 1360 ms for KH3−CT15. The $T_{1\rho}$ experiments utilized the following ^{15}N delays: 8.026, 24.346, 48.346, 78.586, 98.266, 123.226, 150.586, and 177.946 ms for mutKH3; 8.019, 16.179, 31.539, 48.339, 60.339, 75.219, 96.339, and 120.339 ms for wtKH3; 8.015, 16.175, 48.335, 60.335, 75.215, 96.335, and 120.335 ms for KH3−CT15. $T_{1\rho}$ data were collected in an interleaved manner so as to minimize any effects of sample heating or unavoidable changes in NMR conditions. Sixteen and eight scans per t_1 point were used for T_1 and $T_{1\rho}$ experiments, respectively. Experiment recycle delays of 1.17 and 1.26 s were used T_1 and $T_{1\rho}$ measurements, respectively. Relaxation times were calculated by fitting the delay dependent peak intensities to an exponential decay function with a peak intensity baseline of zero. A nonlinear regression fitting routine employing a Powell optimization was used to accomplish this latter task.

^{15}N-{^1H} NOE values were measured with the water flip-back NOE pulse sequence described by Grzesiek and Bax (*41*). ^{15}N-{^1H} NOE values were calculated from the ratio of peak intensities from experiments performed with and without ^1H presaturation. The unsaturated spectrum was recorded by shifting the proton frequency off-resonance by ~3 MHz during the presaturation period. The saturated and unsaturated experiments were completed an interleaved manner with 32 scans/t_1 point. The pulse train used for saturation had 50 ms delays between 162° pulses and was applied for a total of 3.76 s. An additional recovery delay of 1.13 s was included yielding a total recycle time of 4.89 s for both experiments. This relaxation delay is long given proton T_1 values of ~1−1.5 s. However, reported ^{15}N-{^1H} NOE values were corrected as previously described to compensate for the effects of incomplete ^1H magnetization recovery (*41*).

Amide Proton Exchange Experiments. 99.9% D_2O was added to lyophilized samples, and amide proton exchange rates were determined from the rate of disappearance of amide proton peak intensities in ^1H-^{15}N HSQC (*42*) spectra recorded at various time intervals on a Bruker DMX600. All samples were prepared in an ice-bath. Spectra were recorded at 24, 35, 50, 77, 127, and 164 min for wtKH3, 11, 22, 35, 79, 126, and 173 min for mutKH3, and 10, 23, 35, 60, 81, 133, and 201 min for KH3−CT15. These intervals were calculated from the time the sample was placed in the magnet to the midpoint of the HSQC experiment. Small amounts of exchange occurring at the lower temperatures were not considered. Experiments were performed at 300 K for wtKH3 and mutKH3 and at 306 K for KH3−CT15. The uncorrected pH values measured after experiment completion were 4.3, 4.8, and 6.0 for wtKH3, mutKH3, and KH3−CT15, respectively.

RESULTS

Secondary Structure of KH3−CT15. Sequential and medium-range NOEs and secondary ^{13}C chemical shifts for KH3−CT15 are shown in Figure 1. It is clear that wtKH3 retains a $\beta\alpha\alpha\beta\beta\alpha$ topology upon CT15 binding. CBCA(CO)-NH, HNCACB, and 3D ^{15}N separated NOESY (100 ms mixing time) experiments were used to accomplish the backbone assignment. NOE information shown in Figure 1 is either from the 3D ^{15}N separated NOESY or a 4D ^{15}N/^{13}C separated NOESY (120 ms mixing time) (*43*−*45*).

CT15 Inspired wtKH3 Backbone Chemical Shift Differences. A NMR sample of ^{15}N labeled wtKH3 was titrated with a solution of CT15 (see Materials and Methods for conditions) to obtain an estimate of the dissociation constant (K_D) for the complex and to verify the stoichiometry. Backbone ^{15}N and $^1H^N$ chemical shifts were measured throughout the course of this titration by ^1H-^{15}N HSQC experiments (*42*). Many HSQC resonances disappeared during the titration, making it impossible to follow the chemical shifts of those residues. This is likely due to the fast exchange between the free and bound states of KH3. Seventeen residues maintained narrow line widths and had measurable chemical shift changes throughout the titration. Chemical shift values of these latter residues were used to estimate K_D for the complex. Titration data for three of these residues are shown in Figure 2. A nonlinear regression analysis similar to that described by Lian and Roberts (*46*) determined a value of 48 ± 44 μM for the K_D. Note that the chemical shift changes saturate at a concentration slightly greater than a CT15:wtKH3 mole ratio of 1:1 as a result of weak binding, but confirming the 1:1 stoichiometry of the complex. The estimate of this value is important as it explains the lack of any wtKH3-to-CT15 NOE contacts in several attempted 3D ^{13}C-separated/^{12}C-filtered NOESY experiments (*47*).

Nevertheless, perturbations of chemical shifts upon binding provide valuable insight into the nature of the protein-nucleic

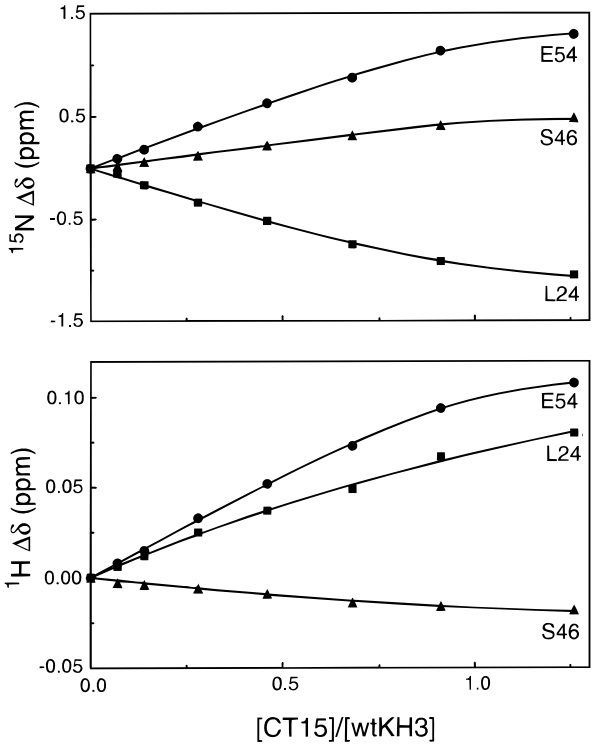

FIGURE 2: Backbone amide chemical shift as a function of CT15 concentration for three wtKH3 residues exhibiting measurable changes. The solid lines were calculated from best fits of the data to an equation similar to that described by Lian and Roberts (*46*). ^{1}H-^{15}N HSQC experiments performed at 33 °C and a ^{1}H frequency of 600 MHz were used to monitor the progress of the titration. Additional titration conditions are described in the Experimental Section.

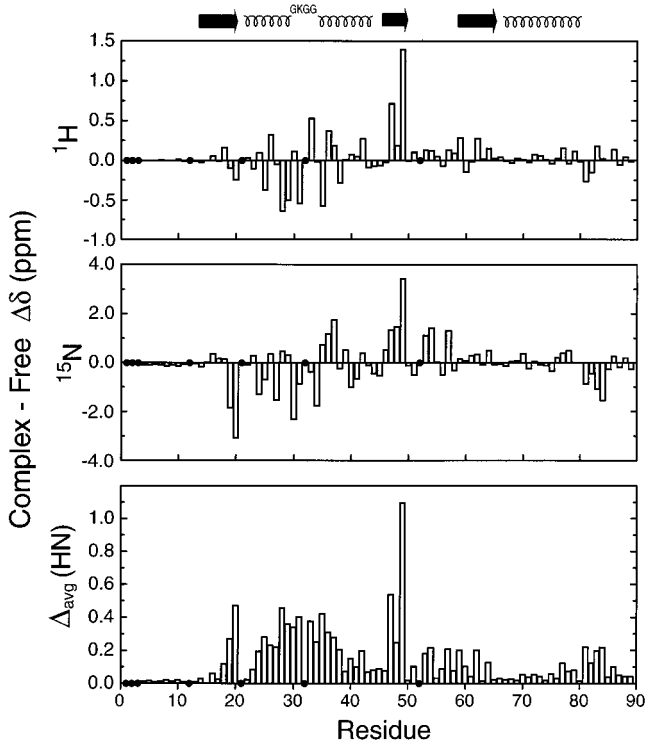

FIGURE 3: Backbone chemical shift differences between CT15-bound wtKH3 present at the end of the titration and free wtKH3. Nonobservable residues are indicated by filled circles at 0 ppm. The weighted average chemical shift differences shown in the lower plot were calculated as described by Garrett et al. (*74*) (i.e., $\{[(\Delta H)^2 + (\Delta N/5)^2]/2\}^{1/2}$) for each ^{1}H/^{15}N pair. Secondary structural elements of mutKH3 are shown at the top of the figure.

acid interactions (*48*−*52*). Backbone ^{15}N and ^{1}H^{N} chemical shift differences between free and CT15-bound wtKH3 are presented in Figure 3. For convenience, the weighted average values have been mapped onto GRASP (*53*) worm and surface representations of the mutKH3 structure shown in Figure 4. A ^{15}N separated 3D-NOESY was sufficient to assign the free wtKH3 backbone resonances as most had values nearly identical to that of the G26R mutant KH3 (mutKH3) for which assignments and a structure have been determined. Naturally, only resonances near the point of mutation had significantly different chemical shift values (data not shown).

On the basis of the G26R mutation's abrogating effect on binding, the distribution of basic residues, and a comparison with the bovine papillomavirus E2 DNA-binding domain (*30*), we previously suggested that KH3's interaction with DNA would be localized to helices α1 and α2 as well as the highly conserved GxxG motif (GKGG for KH3) connecting these two helices (*28*). Musco et al. (*29*) postulated the involvement of the GxxG region based on its conservation in KH domains and ^{15}N relaxation results indicating conformational flexibility in this region. It is clear that Figures 3 and 4 support these hypotheses at least with respect to the interaction of wtKH3 with CT15. Backbone ^{15}N and ^{1}H^{N} resonances of both α1 and α2 are significantly perturbed by the protein's interaction with CT15. One may have anticipated a larger effect for resonances in the GxxG region. Residue G32 of this loop was unfortunately not observed in free wtKH3 at the pH* (5.5) for these experiments. Residue I49 in the *β*2 strand exhibits the largest measurable chemical shift perturbation. K48 and I47 on this same strand also exhibit respectable changes. Therefore, CT15 apparently interacts with the surface of wtKH3 comprised of α1, α2, *β*2, and the GKGG loop. It is interesting to note that T19 and I20 also exhibit sizable chemical shift differences.

Backbone ^{15}N Relaxation Measurements. Backbone ^{15}N dynamics data for mutKH3, wtKH3, and the complex KH3−CT15 are presented in Figure 5. Relaxation data for residues D8, G32, D58, G65, and Q71 of mutKH3, Y6, D8, Q17, K22, K31, H41, Q71, and N79 of wtKH3, and T19, Q71, L76, N79, Q83, and Y84 of KH3−CT15 could not be reliably obtained as a result of spectral overlap. Gly1 and Ser2 resonances were not observed nor are they of any interest since the N-terminus is flexible and disordered in all cases. No backbone relaxation data were obtained for prolines 3, 12, 21, and 52. Additionally, the KH3−CT15 I49 resonance was too weak to reliably make relaxation measurements. T_2 values were calculated from corresponding $T_{1\rho}$, T_1, and chemical shift values, spin lock field strength, and, ^{15}N carrier frequency using the relationship previously described (*54*, *55*).

T_1 and T_2 data were fit to isotropic, axially symmetric, and completely anisotropic models for each system studied as described previously (*55*−*58*). Residues with ^{15}N-{^{1}H} NOE values less than 0.65 and/or identified below as undergoing slow (microsecond to millisecond) chemical exchange were excluded from these calculations. The lowest energy previously published mutKH3 structure was used in all structure dependent fits. It is later revealed that this structure approximation of the backbone is excellent for both

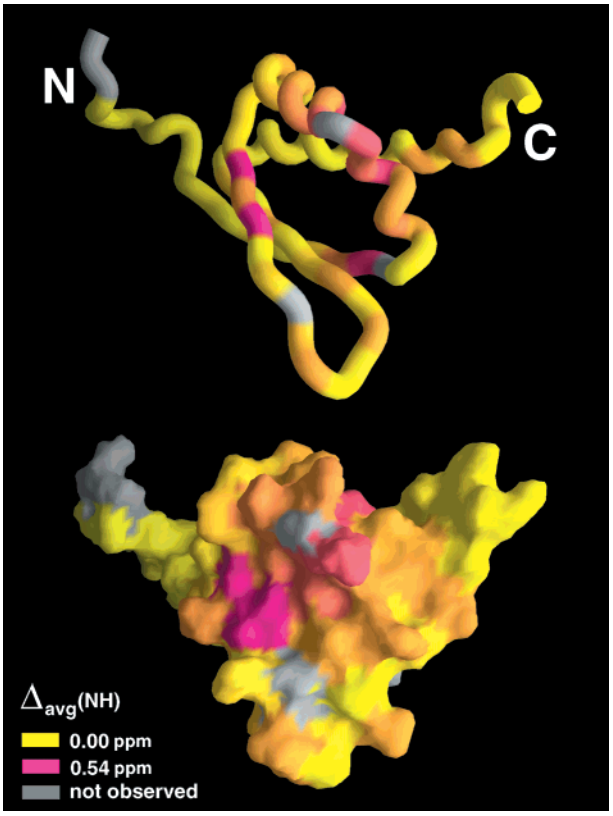

FIGURE 4: Weighted average chemical shift differences shown in Figure 3 mapped onto GRASP (*53*) worm and surface representations of mutKH3 (PDB accession number 1khm). The value of I47, 0.54 ppm, was selected to provide the best contrast. Residues for nonobservable chemical shifts (i.e., prolines and G32) are shown in gray. Note that the N- and C-termini are flexible and nonstructured. Both representations have the same orientation.

wtKH3 and KH3−CT15. The axially symmetric model was determined to be statistically appropriate for each case as judged by F-tests (*59*) comparing the error in the fit for this model to those obtained for fits of the other two. Global parameters derived from the axially symmetric fits are shown in Table 1(order parameters and correlation times for the fast internal motions are presented as Supporting Information). Average T_1, T_2, and ^{15}N-{^{1}H} NOE values for the subsets of data used in these analyses are also included in Table 1.

The overall correlation times for mutKH3 and wtKH3 agree with that measured by Musco et al. (*29*) (6.28 ± 0.036 ns) for KH1 of FMR1. Larger correlation times are expected for KH3 since the fragments studied are 14 residues longer than FMR1 KH1. However, all of these values are slightly higher than ones typically measured for proteins the size of KH3. The relaxation parameters for the free forms of KH3 are concentration and pH dependent (data not shown). Despite efforts to produce sample conditions that optimize monomer concentration, there is probably a small percentage of self-associated KH3 molecules that globally affect the measured relaxation parameters and, therefore, correlation times. Consequently, the difference between the overall correlation times calculated for mutKH3 and wtKH3 is attributed to a difference in the percentage monomer for each sample. However, our interests are in the biologically relevant differences between the internal dynamics of the free and ssDNA-bound protein. The semiquantitative comparisons made in this report are not affected by this small amount of aggregation.

The fitting errors (*E*/*N*) listed in Table 1 are calculated in part from the numerical precision of the relaxation data. Two experiments were performed for each set of data, and the precision of each set was defined as one-half of the corresponding pairwise average rms value (*60*). T_1 and T_2 % errors determined in this manner were, respectively, 1 and 1% for mutKH3, 1 and 1.4% for wtKH3, and 1.2 and 2.2% for KH3−CT15. Factors that might bias the final *E*/*N* values have to be considered to allow the comparison of the goodness of fit for all three cases. These factors include underestimates of experimental errors, different aggregation states of the samples, and the appropriateness of the structure used in the fits. The large *E*/*N* values (>1) suggest that perhaps the reproducibility error underestimates the true experimental error. However, all error estimates were computed in an identical manner permitting a relative comparison of the *E*/*N* values in Table 1. A priori, one might anticipate the average fitting error for mutKH3 to be lower than that of wtKH3 since all sets of data are fit to a mutKH3 structure. Table 1 shows that the opposite is true. wtKH3 has the lower correlation time, suggesting that, of the two, it is the one with the highest percentage of monomer. The model used for the fits assumes a single entity. Therefore, the significant discrepancy in fitting errors between wt- and mutKH3 is the result of differences in aggregation states. *E*/*N* values for wtKH3 and KH3−CT15 are comparable, suggesting that both are equally well fit using the mutKH3 structure. This provides additional evidence that there is no significant change in the backbone of KH3 upon binding CT15.

Identification of wtKH3 & KH3−CT15 Residues Undergoing Chemical Exchange. Backbone ^{15}N T_2 values are only mildly dependent on fast internal motions. However, chemical exchange on the microsecond to millisecond time scale can make a large contribution to this relaxation parameter. Residues of wtKH3 and KH3−CT15 undergoing chemical exchange were identified by consideration of several data presentations.

For nonisotropic diffusion, a ^{15}N T_1/T_2 ratio depends on the orientation of the NH bond vector relative to the rotational diffusion tensor (*61*). Tjandra et al. (*62*) demonstrated that T_1/T_2 ratios can be utilized as restraints in structure calculations for systems with large rotational diffusion anisotropy. The rotational diffusion anisotropy of mutKH3 and wtKH3 is approximately 1.4. This value is large enough to reveal a clear dependence of ^{15}N T_1/T_2 ratios on the orientations of NH bond vectors relative to the rotational diffusion tensor. Significant exchange contributions to ^{15}N T_2 values destroy this direct dependence by shortening T_2 and thus increasing the corresponding T_1/T_2 ratio from that expected by relative bond vector orientation alone. Most proteins possess a high content of regular secondary structure. Consequently, they have a nonrandom distribution of backbone NH bond vectors and, therefore, T_1/T_2 ratios. KH3 presents an interesting case in this regard. Helices α2 and α3 and the strands of the β-sheet are all nearly parallel to the long axis of the rotational diffusion tensor of wtKH3 (and mutKH3). Backbone NH bond vectors for helical residues are parallel to the long axis of the helix. For β-strands, these bond vectors are perpendicular to the direction of the strand. For macromolecules

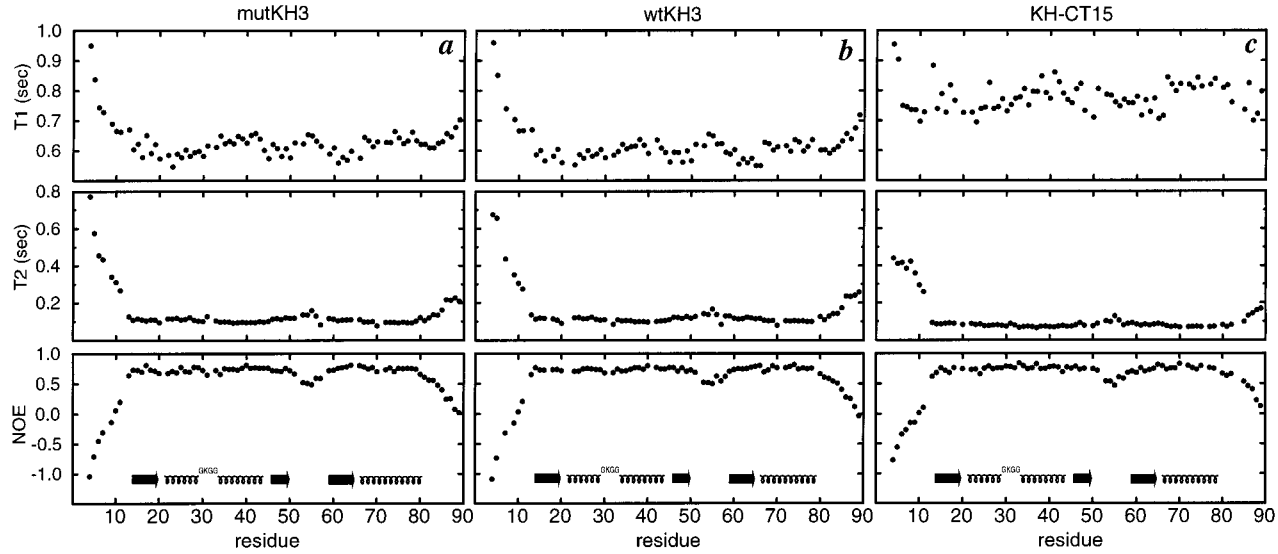

FIGURE 5: ^{15}N relaxation data measured at 60.8 MHz for (a) 0.64 mM ^{15}N-labeled mutKH3 at pH* 4.0, 27 °C, (b) 0.64 mM ^{15}N-labeled wtKH3 at pH* 4.0, 27 °C, and (c) 0.65 mM ^{15}N-labeled wtKH3, 0.70 mM CT15 at pH* 5.5, 33 °C. T_2 values were calculated from $T_{1\rho}$ values as previously described (*54*, *55*). Average errors of these values estimated for rigid regions of the protein are listed in the footnotes of Table 1. Secondary structural elements of mutKH3 are shown at the bottom of each figure.

Table 1: Results of Axially Symmetric Model Fits[a] and Average Backbone ^{15}N Relaxation Observables[b]

	mutKH3	wtKH3	KH3−CT15
Θ (deg)	86 ± 1	85 ± 1	76 ± 1
Φ (deg)	189 ± 1	195 ± 1	191 ± 1
τ_C (ns)	6.74 ± 0.02	6.47 ± 0.01	9.38 ± 0.02
$D_\parallel/D_\perp$	1.46 ± 0.01	1.42 ± 0.01	1.40 ± 0.01
E/*N*	5.9 ± 0.6	3.3 ± 0.4	3.2 ± 0.2
$\langle T_1 \rangle$ (s)	0.611 ± 0.029	0.595 ± 0.025	0.777 ± 0.042
$\langle T_2 \rangle$ (s)	0.106 ± 0.009	0.112 ± 0.009	0.0787 ± 0.0073
⟨NOE⟩	0.738 ± 0.036	0.745 ± 0.030	0.750 ± 0.039

[a] The results of the model fits represent averages calculated from 20 fits where 20% of the data was randomly eliminated for each fit. The error associated with each result is the standard deviation of the average. Data for residues with ^{15}N-{^{1}H} NOE values <0.65 and/or determined to have significant chemical exchange contributions to T_2 were excluded from the fits. The following residues were excluded from the following fits: mutKH3, 1−13, 17, 19, 20, 21, 32, 52−58, 65, 70, 71, 80−89; wtKH3, 1−13, 17, 19, 20, 21, 22, 31, 32, 41, 52−58, 70, 71, 79−89; KH3−CT15, 1−13, 19, 21, 49, 52−57, 71, 76, 79−89. Θ and Φ are the angles of the tensor long axis relative to the PDB coordinate system of the lowest energy mutKH3 structure in the 1khm PDB file. τ_C is the overall correlation time, $D_\parallel$ and $D_\perp$ are components of the axially symmetric rotational diffusion tensor, and *E*/*N* represents the average of the error function described in Tjandra et al. (*55*). [b] T_1, T_2, and ^{15}N-{^{1}H} NOE averages were calculated from the same data sets used in the model fits. Though data sets do not represent normal distributions, a standard deviation of the average was calculated for each set and is reported above. Each type of experiment was performed twice and the actual error was set equal to one-half of the relevant pairwise average rms. T_1, T_2, and ^{15}N-{^{1}H} NOE average % errors calculated in this fashion were, respectively, 1.0, 1.0, and 2.1 for mutKH3, 1.0, 1.4, and 2.2 for wtKH3, and 1.2, 2.2, and 2.0 for KH3−CT15.

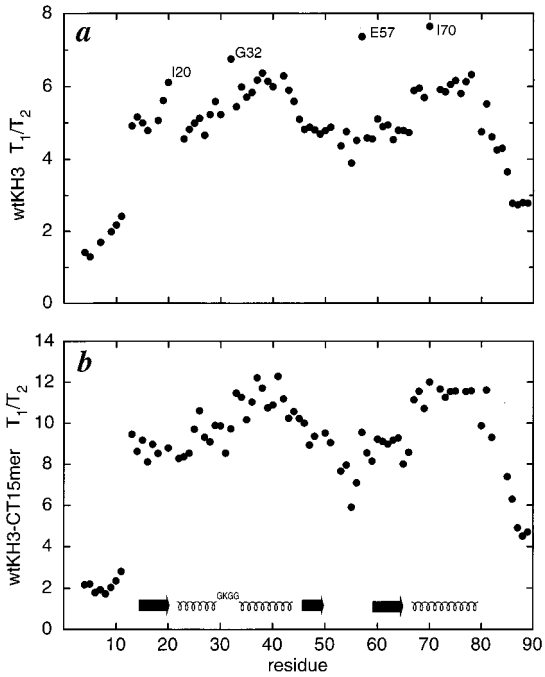

FIGURE 6: Pairwise ratios of T_1 and T_2 values shown in Figure 5 for (a) wtKH3 and (b) KH3−CT15. Secondary structural elements of mutKH3 are shown at the bottom of panel b.

with anisotropic rotational diffusion, T_1/T_2 values are at a maximum and minimum for NH bond vectors parallel and perpendicular, respectively, to the long axis of the rotational diffusion tensor as shown previously (*62*). Therefore, one expects large T_1/T_2 values for residues in helices α2 and α3 and small ones for residues in the β-sheet of unbound KH3. Figure 6a verifies this latter fact. Residues in helices α2 (aa 34−43) and α3 (aa 67−79) have large, comparable T_1/T_2 ratios where residues in the β-sheet (aa 14−20, 46−50, 60−65) are near the lower extreme. In the wtKH3 case (Figure 6a), residues I20, G32, E57, and I70 are immediately suspicious due to their apparent anomalously large magnitude. I20 and I70 are particularly noteworthy as these residues are in regions of regular secondary structure and one expects their ratios to be similar in magnitude to those of their respective sequential neighbors. Consequently, I20 and I70 certainly undergo chemical exchange on the microsecond to millisecond time scale. Examination of the mutKH3 structure reveals that the NH bond vector of G32 is more perpendicular than parallel to the long axis of the rotational diffusion tensor. Therefore, a large ratio is not expected for G32 and chemical exchange of this residue is concluded. One cannot make similar structure-based conclusions about E57 as this residue

is in a less well-defined region of the protein. T19 of wtKH3 also appears to have a larger than expected ratio. So, at present, T19, I20, G32, E57, and I70 are thought to be potentially involved in slow chemical exchange for wtKH3. Figure 6b reveals similar overall features for KH3−CT15. It is not too surprising that KH3 in the bound form has structural similarities to the free form, but there is certainly no a priori reason to think that the rotational diffusion tensors might be similar. No clear candidates for chemical exchange are evident for KH3−CT15 in Figure 6b.

More general statistical methods which exclude explicit secondary structure considerations, but are otherwise analogous, are often used to identify residues undergoing chemical exchange when other experimental data are not available. The method employed by Barbato et al. (*36*) with a T_2 cutoff of 1.5 ± SD was used for all three present cases. This method indicated possible chemical exchange for residues G32, E57, and I70 of wtKH3. No residues for KH3−CT15 were identified. Note that residues in both termini (aa 1−13 and 80−89) were excluded from this analysis.

A third method to identify residues undergoing chemical exchange was also utilized. Macromolecules dissolved in dilute liquid crystals experience a slight alignment allowing the measurement of residual dipolar couplings (*63*). Furthermore, ^{1}H-^{15}N dipolar couplings are correlated with ^{15}N T_1/T_2 ratios when a neutral liquid crystal medium is used. Dipolar couplings depend on the orientation of the bond vector relative to the molecular alignment tensor, and as stated above, ^{15}N T_1/T_2 ratios depend on the orientation of the time-average NH bond vector relative to the molecule's rotational diffusion tensor. Therefore, a correlation between the two classes of information occurs when the alignment tensor and diffusion tensor have similar orientations (*64*). ^{15}N T_1/T_2 data for wtKH3 and KH3−CT15 plotted against the dipolar couplings previously measured for mutKH3 are shown in Figure 7. Exchange suspects identified by the previous statistical method are labeled. Unfortunately, of the residues suspected of slow chemical exchange, dipolar couplings could only be measured for I20 and I70: residues T19 and E57 are missing from these comparisons as a result of spectral overlap in the liquid crystal system, and G32 is not observed at the sample pH and temperature used for the dipolar coupling measurements.

Figure 7a reveals that I20 and I70 of wtKH3 clearly undergo backbone exchange. The T_1/T_2 ratio is larger than that expected from the dipolar coupling, indicating a T_2 shortened by exchange. Exchange contributions to transverse relaxation rates, $R_{2,exch}$, calculated from the deviation from the line in Figure 7a and appropriate dipolar couplings are 2.1 s^{-1} for I20 and 3.3 s^{-1} for I70. $R_{2,exch}$ values were also estimated from T_2 values determined by fits of respective T_1 and ^{15}N-{^{1}H} NOE values to the mutKH3 structure using the global relaxation parameters derived from the axially symmetric model fit. The difference between the calculated R_2 and the observed R_2 was used to determine $R_{2,exch}$ values of 2.5 s^{-1} for I20 and 2.9 s^{-1} for I70. Clearly, the agreement between the two different methods of determining $R_{2,exch}$ is quite good. The latter method yielded $R_{2,exch}$ values of 1.3, 3.6, and 4.4 s^{-1} for T19, G32, and E57, respectively.

The correlation between KH3−CT15 T_1/T_2 ratios and mutKH3 dipolar couplings shown in Figure 7b is much worse than that demonstrated in Figure 7a. In fact, there is no a priori reason to expect any correlation as the global shape of the complex is likely to be different than that of the free protein. Small CT15 induced structural changes for the wtKH3 also lead to a poorer correlation. However, a moderate amount of correlation does exist and no obvious candidates for exchange are evident. (I70 and K37 are tending toward high T_1/T_2 ratios, but their deviation from the correlation cannot be considered statistically significant.) Of course, residues with small exchange contributions to T_2 are less likely to be discovered in this poorly correlated set of data, but residues with large T_2 exchange contributions should still be evident.

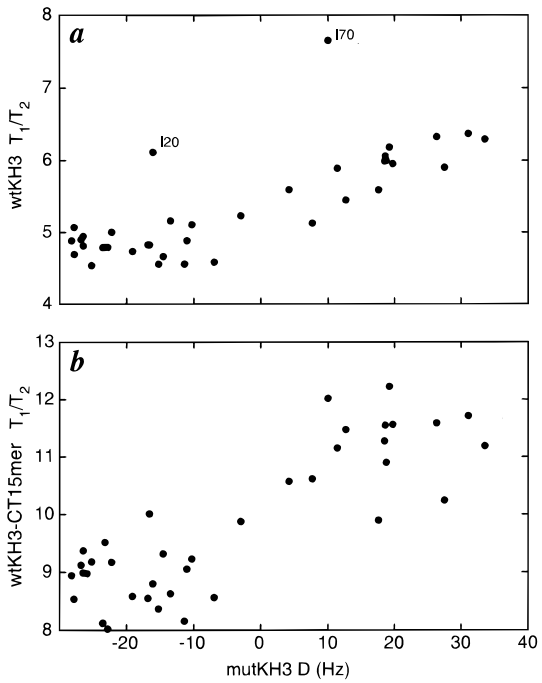

FIGURE 7: Pairwise plot of T_1/T_2 ratios vs mutKH3 residual dipolar couplings measured in Baber et al. (*28*) for wtKH3 and CT15-bound wtKH3. Residues with backbone ^{15}N-{^{1}H} NOE values < 0.65 were excluded from these plots.

To summarize, residues I20, G32, E57, and I70 are unambiguously identified as undergoing chemical exchange on the microsecond to millisecond time scale for wtKH3. T19 is also included in this subset because of it's elevated T_1/T_2 ratio, proximity to I20, and a large error (>3 SDs) in the axially symmetric model fit. No residues undergoing exchange were identified for KH3−CT15. The same analysis performed on mutKH3 revealed that residues Q17, T19, I20, E57, and I70 of this protein undergo exchange. Note that any residues not included in both wtKH3 and mutKH3 lists (i.e., Q17 and G32) were missing from the analysis as a result of spectral overlap.

wtKH3 and mutKH3 Comparisons. A pairwise plot of wtKH3 ^{15}N T_1/T_2 ratios versus mutKH3 ratios is shown in Figure 8. As noted earlier, a ^{15}N T_1/T_2 ratio depends on the orientation of the time-averaged NH bond vector relative to the rotational diffusion tensor for nonisotropic diffusion. Therefore, the excellent correlation shown in Figure 8 demonstrates that the wild-type and mutant KH3 backbone structures are nearly identical. This relationship is clearly not 1-to-1: a least-squares fit of the data yields a slope of 0.84. This deviation is a result of the 0.27 ns difference in correlation times discussed above. The two notable outliers

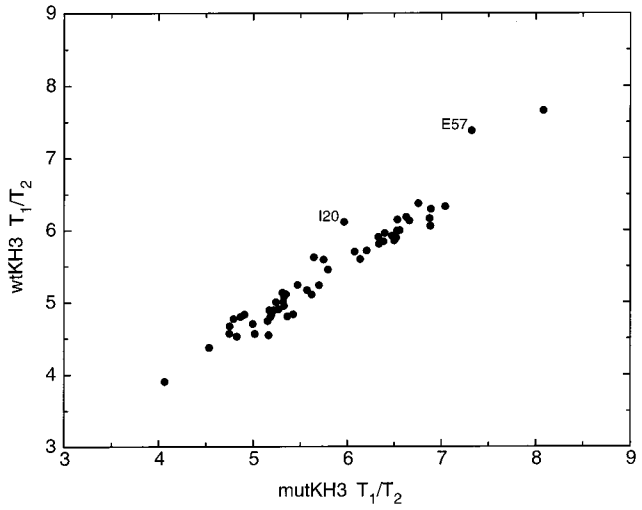

FIGURE 8: Comparison of wtKH3 and mutKH3 ^{15}N T_1/T_2 ratios. Values for residues 1−13 and 80−89 are not shown. The slope and correlation coefficient of the line least-squares fit to these data are 0.84 and 0.98, respectively (I20 and E57 were excluded from this fit). The average T_1/T_2 error is 1.4% for mutKH3 and 1.7% for wtKH3.

in Figure 8 are I20 and E57. The lessened correlation between these two ratios could be due to differences in the time-averaged NH bond vector orientations. However, residues I20 and E57 were identified as undergoing chemical exchange in both cases. A direct comparison of relaxation data for both proteins reveals that the unexpected difference in T_1/T_2 values for I20 is due to a difference in T_2 values. Therefore, the reduced correlation of I20 shown in Figure 8 is probably due to a difference in the chemical exchange process. A structural explanation for this difference in exchange rates cannot be offered without further studies. An exchange rate of 1.8 s^{-1} was calculated for I20 of mutKH3 based on the correlation between mutKH3 T_1/T_2 ratios and mutKH3 dipolar couplings ($R_{2,exch}$ = 2.1 s^{-1} for I20 of wtKH3 as previously noted). This latter correlation is comparable to that shown in Figure 7a as inferred from the results in Figures 7a and 8. In the case of E57, small differences in both T_1 and T_2 conspire to produce the unexpected difference in T_1/T_2 values between wt- and mutKH3. Consequently, it is impossible to identify a single physical origin for the difference in T_1/T_2 ratios for E57. No additional significant dynamics differences between wtKH3 and mutKH3 were noted in direct comparisons of relaxation data.

Comparison of wtKH3 and KH3−CT15 Dynamics. The ^{15}N-{^1H} NOE values for residues in the β-hairpin (residues 51−58) connecting $\beta1$ and $\beta2$ are lower than average in all three cases (Figure 5). Liang et al. (*65*) also measured reduced ^{15}N-{^1H} NOE values in the comparable region of the human papillomavirus-31 (HPV-31) E2 DNA-binding domain (DBD). They suggested that such flexibility is necessary for specific DNA recognition. Furthermore, by analogy to several other dynamics studies of protein−nucleic acid interactions and comparison with the dsDNA−bovine papillomavirus (BPV) E2 complex, they noted that this loop probably becomes less flexible upon binding. Comparison of ^{15}N-{^1H} NOE values for wtKH3 (Figure 5b) and KH3−CT15 (Figure 5c) reveals no statistically significant change in NOE values of the β-hairpin upon CT15 binding. However, T_1 values in this region are altered upon complex formation. For residues 14−78 excluding 54−57, the average pairwise ratio of KH3−CT15 T_1 values to wtKH3 T_1 values is 1.31 ± 0.03 whereas the average of the ratios for residues 54−57 in the β-hairpin is 1.20 ± 0.03. Both classes of relaxation data, ^{15}N-{^1H} NOE and T_1, are dependent on the fast (picosecond to nanosecond) internal motions. In the Lipari-Szabo model (*57*, *58*), the internal correlation time, τ_e, makes a larger contribution to the final NOE value than the corresponding fast internal order parameter, S_f^2. The opposite is true for T_1 values: S_f^2 has more relative importance than τ_e (*66*). Therefore, within this model, complex formation results in no measurable change of the average τ_e for residues in the β-hairpin, but the average S_f^2 for residues 54−57 is increased by approximately 8%. In the case of BPV E2 DBD, a residue in the β-hairpin, R370, was shown to directly interact with the dsDNA (*30*), making it easier to visualize reduced motion for this region in the bound form. However, for wtKH3, one cannot deduce whether the observed change is the result of direct contact of this loop with the ssDNA or increased steric hindrance brought about slight conformational changes in other parts of the molecule. Four of the nine residues in the β-hairpin of wtKH3 are acidic, which makes direct DNA contact with the middle region of this loop seem unlikely. This is further supported by a small chemical shift perturbation (Figure 3) in the β-hairpin region.

The GKGG loop connecting helices α1 and α2 is a highly conserved motif (GxxG) in the KH family. CT15-induced changes in ^{15}N-{^1H} NOE and T_1 values of this loop are just the opposite of those described for the β-hairpin: the average ^{15}N-{^1H} NOE value in this region is affected whereas the average T_1 is not. The average pairwise ratio of KH3−CT15 NOEs to wtKH3 NOEs for residues G30, G32, G33, and Q34 is 1.13 ± 0.02, whereas the average for residues 14−78 excluding 30−34 is 1.00 ± 0.05. While elevated differences for one or two residues in the GxxG region are not statistically significant, the trend of four residues in this region experiencing above-average positive NOE differences upon binding is undeniable. Therefore, within the confines of the Lipari-Szabo model, CT15 binding has no measurable affect on the fast internal order parameter, S_f^2, but decreases the corresponding effective internal correlation time by approximately 70%. All previous considerations as well as the above chemical shift perturbation data suggest that the GKGG loop is likely to be a region of direct DNA interaction. A change in the local fast dynamics of this loop is consistent with this latter interpretation. Note that the effects of overall correlation time differences between the bound and unbound wtKH3 were considered when analyzing changes in backbone dynamics of both the GKGG loop and the previously discussed β-hairpin.

Attention is now focused on a direct comparison between wtKH3 and KH3−CT15 T_2 values. The pairwise ratios (excluding residues 1−13, 80−89, 20, 32, 57, and 70) of KH3−CT15 T_2 values to wtKH3 T_2 values are generally constant with an average of 0.70 ± 0.04. There are no noteworthy outliers on the lower side of this average. However, the T_2 ratios for residues I20, G32, E57, and I70 are significantly larger than this average with values 0.90, 0.92, 0.95, and 0.86, respectively. As these values are anomalously large, the four T_2 values are disproportionally smaller in the free protein than in the bound form. Note that these four

residues were earlier identified as undergoing chemical exchange in the free protein, and no clear evidence for similar behavior in the complex was observed. Therefore, upon CT15 binding, chemical exchange rates for I20, G32, E57, and I70 are significantly reduced. Parameters for the fifth residue of exchange interest, T19, were not measurable in the KH3−CT15 case as a result of spectral overlap.

Amide Proton Exchange. The results of wtKH3 and KH3−CT15 amide proton exchange experiments are shown in panels a and b of Figure 9, respectively. The protection factors (*67*) presented were calculated by the method of Bai et al. (*68*). For wtKH3 and KH3−CT15, numerical estimates of protection factors are not given for resonances that disappeared after 35 min (fast exchange) and those that decreased in intensity by less than 25% by the last time interval (slow exchange). It is clear that the C-terminal helix, α3, and residues in the β-sheet (residues 14−20, 46−49, and 59−65) are more stable than other regions of the protein. Rates are immeasurably fast for residues in the N- and C-termini (residues 4−13 and 79−89), in the β-hairpin (*51*−*58*) and in the conserved GxxG loop (*30*−*33*). The moderate protection factor for A45 and structure examination suggest that the amide proton of A45 probably hydrogen bonds with the side chain of S43. Large protection factors for T66 and Q69 confirm a N-capping box for the C-terminal helix. Secondary chemical shifts previously presented for mutKH3 and for CT15-bound wtKH3 (Figure 1) also indicate the presence of a N-capping box for α3 (*69*). Most interesting, however, are the results for helices α1 and α2. Amino acids in these helices exchange fast compared to those in α3 and the β-sheet. Therefore, α1 and α2 are destabilized with respect to other secondary structural elements. Secondary structure information for mutKH3 (*28*) and KH3−CT15 (Figure 1), including secondary Cα and Cβ chemical shifts, NOE patterns, and H^N-Hα scalar coupling constants, define the existence of these two helices. The ^{15}N relaxation data for helices α1 and α2 previously discussed are consistent with that of other regions of stable secondary structure. Therefore, these two helices must undergo a very slow local unfolding that results in relatively lower protection factor values.

Protection factors for the KH3−CT15 are shown in Figure 9b. Pairwise ratios of quantifiable protection factors for wtKH3 and KH3−CT15 are shown in Figure 9c to make the comparison of panels a and b in Figure 9 easier. It is expected that regions of the bound wtKH3 not protected by the ssDNA interaction will exchange faster than comparable regions of the free wtKH3 as a result of pH* (6.0 for KH3−CT15 vs 4.3 for wtKH3) and temperature (33 °C for KH3−CT15 vs 27 °C for wtKH3) differences. However, protection factors should account for pH and temperature differences, making the data sets presented directly comparable (*68*). Figure 9c reveals that residues in the C-terminal helix and at the beginning of β1 exhibit the smallest changes in protection factors upon binding ssDNA whereas most residues in regions of regular secondary structure experience substantial increases. Unfortunately, this information does not reveal whether these increases are the result of physical shielding by the CT15 or an increase in secondary structure stability. Residues in α2 and those involved in the β-sheet hydrogen-bonding network excluding the N-terminal half of β1 show similarly large $P_{KH3-CT15}/P_{wtKH3}$ ratios. I29 of α1

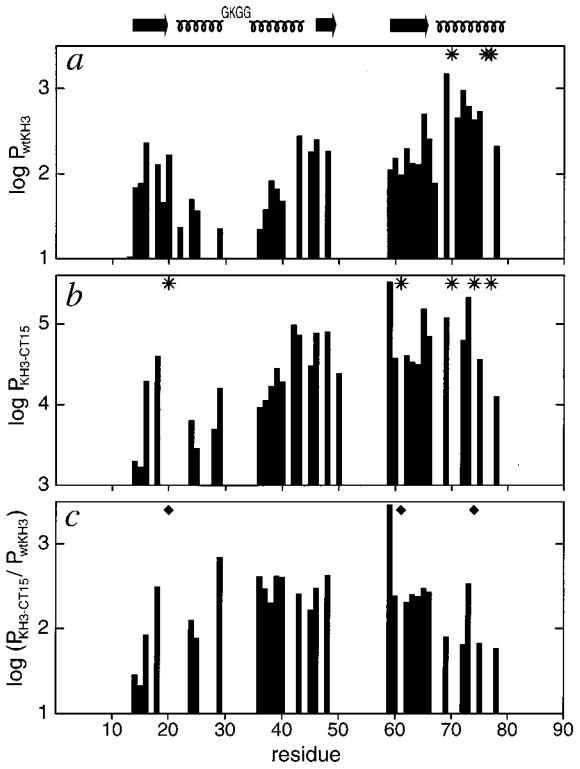

FIGURE 9: Results of backbone amide proton exchange experiments. $P = k_{rc}/k_{obs}$ where k_{rc} is the random coil amide proton exchange rate calculated by the method described by Bai et al. (*68*) and k_{obs} is the observed rate. Logs of the pairwise ratios of protection factors of KH3−CT15 and wtKH3 are plotted in panel **c**. Stars indicate amide protons that exchange too slowly to estimate an exchange time (i.e., < 25% change in amide proton intensity by the end of the experiment). Diamonds in panel c indicate residues for which exchange is definitely slower in the CT15-bound form, but for which an actual ratio cannot be calculated. Secondary structural elements of mutKH3 are shown at the top of the figure. Experiments were performed at 27 °C and uncorrected pH of 4.3 for wtKH3 and at 33 °C and uncorrected pH of 6.0 for KH3−CT15.

shows a substantial increase in its protection factor upon CT15-binding, but resonances for I27 and G26 are still not observable and the $P_{KH3-CT15}/P_{wtKH3}$ ratio for A25 is similar to those of α3. It was hoped that CT15 binding might allow the measurement of exchange rates for amide protons of residues 30−35 (30−33 comprise the conserved GxxG motif), I47, and I49 as well as those of any side-chain amino groups that might interact with the oligonucleotide. However, amide protons for these residues are either still solvent accessible in the bound form or are so labile that they exchange completely when the ssDNA transiently dissociates. The latter possibility is plausible since the complex has a large K_D. No significant differences in the protection factors for wtKH3 and mutKH3 were observed.

DISCUSSION

The secondary structure information for KH3−CT15 (Figure 1) and good fits of KH3−CT15 bacbone ^{15}N relaxation data to a mutKH3 structure (Table 1) show that KH3 does not undergo any global structural change upon CT15 binding. Chemical-shift perturbations (Figure 2) indicate that a large portion of wtKH3 is involved in binding the CT15 with residues in α1, α2, the GKGG loop connecting α1 and α2, β2, and the C-terminal end of β1 exhibiting the largest changes. ^{15}N relaxation results show that CT15 interaction

alters fast backbone motions of wtKH3 residues in the GKGG region and in a portion of the β-hairpin (residues 54−57). These results also indicate that the CT15 affects chemical exchange on a microsecond to millisecond time scale for residues I20, G32, E57, and I70. Amide proton-exchange experiments reveal α1 and α2 to be less stable than other regions of regular secondary structure for all three cases. These latter experiments additionally indicate that a large portion of wtKH3 is protected from solvent in some manner when the protein is bound to the CT15.

Sites of CT15 interaction identified by chemical shift perturbation results are consistent with previous hypotheses (*28*, *29*) except for the C-terminal end of β1. Though difficult to envision, it is possible that the CT15 loosely wraps around the β-sheet of wtKH3 to contact residues T19 and I20 of β1. Consistent with this latter idea are the amide proton-exchange results that indicate protection of this β-sheet. However, ^{15}N relaxation results show that I20 (and perhaps T19) undergoes chemical exchange that is altered by the interaction of CT15 with the protein. If the chemical shift differences between the alternate conformations of I20 is significant, then any perturbation that affects the relative populations of I20 conformers could cause a large change in chemical shift. I20 could be a hinge region of the molecule. The differences between I20 relaxation results for wtKH3 and G26R mutant KH3 are consistent with this latter notion as the bulkier Arg side chain could easily alter the chemical exchange (rate or relative conformer populations) at such a hinge site. The presence of neighboring proline P21 is also suggestive as prolines are often found in molecular hinges. Nevertheless, one cannot definitively conclude whether the large CT15-induced chemical shift changes at T19 and I20 are due to oligonucleotide proximity, indirect perturbation of chemical exchange in this region, or, perhaps, a convolution of both effects.

There is notable precedence for the amide proton-exchange results, indicating that α1 and α2 are less stable than other regions of regular secondary structure. Liang et al. (*65*) showed that the recognition helix of HPV-31 E2 DBD also undergoes fast amide proton exchange relative to the more stable C-terminal helix. Furthermore, they cite other proteins that exhibit chemical exchange in their respective DNA-binding regions including the *trp* repressor (*70*), the leucine-zipper motif in GCN4 (*71*), and the *ets* domain of Fli-1 (*72*). The results for KH3, therefore, augment existing evidence for the biological importance of helix instability in DNA recognition. Discussion of the potential relevance of helix instability and related thermodynamic issues have been adequately explored in the references cited above. It was initially thought that the G26R mutation prevented CT15 binding by charge or steric interference (*28*). However, in light of the presumed importance of helix instability for DNA binding, one might hypothesize that this mutation modifies the degree of helix stability and, therefore, the ability of the protein to bind DNA. Current results do not demonstrate any such effects. Any mutationally dependent differences in α1 stability are either on a time scale not probed by these experiments or too subtle to be detected. Nevertheless, there is evidence which suggests that the stability of α1 may vary significantly across the KH family: only one helical turn adjacent to the conserved GxxG region is evident for α1 in KH6 of vigilin (*14*) and only some of the calculated structures of KH1 of FMR1 show the presence of one helical turn (*29*). The α1 helices found in the third KH domains of Nova-1 and -2 (*15*) are both comparable in length to that of mutKH3. The degree and relative importance of this variability in α1 cannot be presently addressed suggesting future studies regarding this issue.

HPV and BPV E2 DBD sequences are not homologous to KH domains. However, our previous work pointed out structural and electrostatic similarities between KH3 and BPV E2 DBD (*28*). Now, general DNA-binding region and dynamical similarities between KH3 and E2 DBDs have been demonstrated. At present, we can only suggest that these similarities are likely nothing more than general, qualitative features of this structural class of nucleic acid binding domains.

We have presented the first view of the interaction of an important class of nucleic acid binding modules with ssDNA. The structure of a Nova protein KH domain−RNA complex was reported (*73*) after the submission of this paper. The general region of RNA interaction of this Nova KH domain is comparable to the ssDNA-binding area of the hnRNP K KH3 module revealed in this work. The full structure of the KH3−CT element complex is a clear, future goal. A major concern is that hnRNP K likely exhibits a much greater affinity to the CT element than KH3 as the result of KH domain cooperativity in binding. It is perhaps true that the low binding affinity of KH3 to the CT15 is an intrinsic effect that cannot be overcome. Nevertheless, we are currently searching for a biologically relevant combination that yields a complex with a smaller, workable K_d under NMR sample conditions.

SUPPORTING INFORMATION AVAILABLE

Tables of measured relaxation data and corresponding order parameters and correlation times for the fast internal motions calculated with an axially symmetric model. This material is available free of charge via the Internet at http://pubs.acs.org.

REFERENCES

1. Michelotti, E. F., Michelotti, G. A., Aronsohn, A. I., and Levens, D. (1996) *Mol. Cell. Biol. 16*, 2350−2360.
2. Tomonaga, T., and Levens, D. (1996) *Proc. Natl. Acad. Sci. U.S.A. 93*, 5830−5835.
3. Takimoto, M., Tomonaga, T., Matunis, M., Avigan, M., Krutzsch, H., Dreyfuss, G., and Levens, D. (1993) *J. Biol. Chem. 268*, 18249−18258.
4. Tomonaga, T., and Levens, D. (1995) *J. Biol. Chem. 270*, 4875−4881.
5. Bomsztyk, K., Van Seuningen, I., Suzuki, H., Denisenko, O., and Ostrowski, J. (1997) *FEBS Lett. 403*, 113−115.
6. Ostareck-Lederer, A., Ostareck, D. H., and Hentze, M. W. (1998) *Trends Biochem. Sci. 23*, 409−411.
7. Wadd, S., Bryant, H., Filhol, O., Scott, J. E., Hsieh, T., Everett, R. D., and Clements, J. B. (1999) *J. Biol. Chem. 274*, 28991−28998.
8. Hsieh, T., Matsumoto, M., Chou, H., Schneider, R., Hwang, S. B., Lee, A. S., and Lai, M. M. C. (1998) *J. Biol. Chem. 273*, 17651−17659.
9. Miau, L., Chang, C., Shen, B., Tsai, W., and Lee, S. (1998) *J. Biol. Chem. 273*, 10784−10791.
10. Collier, B., Goobar-Larsson, L., Sokolowski, M., and Schwartz, S. (1998) *J. Biol. Chem. 273*, 22648−22656.
11. Ostareck, D. H., Ostareck-Lederer, A., Wilm, M., Thiele, B. J., Mann, M., and Hentze, M. W. (1997) *Cell 89*, 597−606.

12. Du, Q., Melnikova, I. N., and Gardner, P. D. (1998) *J. Biol. Chem. 273*, 19877−19883.
13. Dejgaard, K., and Leffers, H. (1996) *Eur. J. Biochem. 241*, 425−431.
14. Musco, G., Stier, G., Joseph, C., Antonietta, M., Morelli, C., Nilges, M., Gibson, T. J., and Pastore, A. (1996) *Cell 85*, 237−245.
15. Lewis, H. A., Chen, H., Edo, C., Buckanovich, R. J., Yang, Y. Y., Musunuru, K., Zhong, R., Darnell, R. B., and Burley, S. K. (1999) *Structure 7*, 191−203.
16. Duncan, R., Bazar, L., Michelotti, G., Tomonaga, T., Krutzsch, H., Avigan, M., and Levens, D. (1994) *Genes Dev. 8*, 465−480.
17. Nagai, K. (1996) *Curr. Opin. Struct. Biol. 6*, 53−61.
18. Ashley, C. T., Jr., Wilkinson, K. D., Reines, D., and Warren, S. T. (1993) *Science 262*, 563−566.
19. Siomi, H., Choi, M., Siomi, M. C., Nussbaum, R. L., and Dreyfuss, G. (1994) *Cell 77*, 33−39.
20. De Boulle, K., Verkerk, A. J., Reyniers, E., Vits, L., Hendrickx, J., Van Roy, B., Van den Bos, F., de Graaff, E., Oostra, B. A., and Willems, P. J. (1993) *Nat. Genet. 3*, 31−35.
21. Swanson, M. S., and Dreyfuss, G. (1988) *Mol. Cell. Biol. 8*, 2237−2241.
22. Matunis, M. J., Michael, W. M., and Dreyfuss, G. (1992) *Mol. Cell Biol. 12*, 164−171.
23. Wang, L. L., Richard, S., and Shaw, A. S. (1995) *J. Biol. Chem. 270*, 2010−2013.
24. Liu, K., and Hanna, M. M. (1995) *J. Mol. Biol. 247*, 547−558.
25. Buckanovich, R. J., and Darnell, R. B. (1997) *Mol. Cell. Biol. 17*, 3194−3201.
26. Chkheidze, A. N., Lyakhov, D. L., Makeyev, A. V., Morales, J., Kong, J., and Liebhaber, S. A. (1999) *Mol. Cell. Biol. 19*, 4572−4581.
27. Doyle, G. A. R., Betz, N. A., Leeds, P. F., Fleisig, A. J., Prokipcak, R. D., and Ross, J. (1998) *Nucleic Acids Res. 26*, 5036−5044.
28. Baber, J. L., Libutti, D., Levens, D., and Tjandra, N. (1999) *J. Mol. Biol. 289*, 949−962.
29. Musco, G., Kharrat, A., Stier, G., Fraternali, F., Gibson, T. J., Nilges, M., and Pastore, A. (1997) *Nat. Struct. Biol. 4*, 712−716.
30. Hegde, R., Grossman, S., Laimins, L., and Sigler, P. (1992) *Nature 359*, 505−512.
31. Bochkarev, A., Barwell, J., Pfuetzner, R., Bochkareva, E., Frappier, L., and Edwards, A. (1996) *Cell 84*, 791−800.
32. Bochkarev, A., Bochkareva, E., Frappier, L., and Edwards, A. (1998) *J. Mol. Biol. 284*, 1273−1278.
33. Delaglio, F., Grzesiek, S., Vuister, G. W., Zhu, G., Pfeifer, J., and Bax, A. (1995) *J. Biomol. NMR 6*, 277−293.
34. Garrett, D. S., Powers, R., Gronenborn, A. M., and Clore, G. M. (1991) *J. Magn. Reson. 95*, 214−220.
35. Marion, D., Ikura, M., Tschudin, R., and Bax, A. (1989) *J. Magn. Reson. 85*, 393−399.
36. Barbato, G., Ikura, M., Kay, L. E., Pastor, R. W., and Bax, A. (1992) *Biochemistry 31*, 5269−5278.
37. Piotto, M., Saudek, V., and Sklenar, V. (1992) *J. Biomol. NMR 2*, 661−665.
38. Bax, A., and Pochapsky, S. S. (1992) *J. Magn. Reson. 99*, 638−642.
39. Grzesiek, S., and Bax, A. (1993) *J. Biomol. NMR 3*, 185−204.
40. Peng, J. W., Thanabal, V., and Wagner, G. (1991) *J. Magn. Reson. 95*, 421−427.
41. Grzesiek, S., and Bax, A. (1993) *J. Am. Chem. Soc. 115*, 12593−12594.
42. Bodenhausen, G., and Ruben, D. J. (1980) *Chem. Phys. Lett. 69*, 185−189.
43. Bax, A., and Grzesiek, S. (1993) *Acc. Chem. Res. 26*, 131−138.
44. Clore, G. M., and Gronenborn, A. M. (1988) *Trends Biotech. 16*, 22−34.
45. Clore, G. M., and Gronenborn, A. M. (1991) *Science 252*, 1390−1399.
46. Lian, L.-Y., and Roberts, G. C. K. (1993) in *NMR of Macromolecules. A Practical Approach* (Roberts, G. C. K., Ed.) pp 153−182, Oxford University Press, Oxford.
47. Ikura, M., Clore, G. M., Gronenborn, A. M., Zhu, G., Klee, C. B., and Bax, A. (1992) *Science 256*, 632−638.
48. Otting, G., Qian, Y. Q., Billeter, M., Muller, M., Affolter, M., Gehring, W. J., and Wuthrich, K. (1990) *EMBO J. 9*, 3085−3092.
49. Chen, Y., Reizer, J., Saier, M. H. Jr., Fairbrother, W. J., and Wright, P. E. (1993) *Biochemistry 32*, 32−37.
50. Gronenborn, A. M., and Clore, G. M. (1993) *J. Mol. Biol. 233*, 331−335.
51. Gorlach, M., Wittekind, M., Beckman, R. A., Mueller, L., and Dreyfuss, G. (1992) *EMBO J. 11*, 3289−3295.
52. Emerson, S. D., Madison, V. S., Palermo, R. E., Waugh, D. S., Scheffler, J. E., Tsao, K.-L., Kiefer, S. E., Liu, S. P., and Fry, D. C. (1995) *Biochemistry 34*, 6911−6918.
53. Nicholls, A., Sharp, K., and Honig, B. (1991) *Proteins 11*, 281−296.
54. Davis, D. G., Perlman, M. E., and London, R. E. (1994) *J. Magn. Reson. B 104*, 266−275.
55. Tjandra, N., Wingfield, P., Stahl, S., and Bax, A. (1996) *J. Biomol. NMR 8*, 273−284.
56. Tjandra, N., Feller, S. E., Pastor, R. W., and Bax, A. (1995) *J. Am. Chem. Soc. 117*, 12562−12566.
57. Lipari, G., and Szabo, A. (1982) *J. Am. Chem. Soc. 104*, 4546−4559.
58. Lipari, G., and Szabo, A. (1982) *J. Am. Chem. Soc. 104*, 4559−4570.
59. Bevington, P. R., and Robinson, D. K. (1992) *Data Reduction and Error Analysis for the Physical Sciences*, 2nd ed., McGraw-Hill, New York.
60. Tjandra, N., Kuboniwa, H., Ren, H., and Bax, A. (1995) *Eur. J. Biochem. 230*, 1014−1024.
61. Woessner, D. E. (1962) *J. Chem. Phys. 36*, 647−654.
62. Tjandra, N., Garrett, D. S., Gronenborn, A. M., Bax, A., and Clore, G. M. (1997) *Nat. Struct. Biol. 4*, 443−449.
63. Tjandra, N., and Bax, A. (1997) *Science 278*, 1111−1114.
64. de Alba, E., Baber, J. L., and Tjandra, N. (1999) *J. Am. Chem. Soc. 121*, 4282−4283.
65. Liang, H., Petros, A. M., Meadows, R. P., Yoon, H. S., Egan, D. A., Walter, K., Holzman, T. F., Robins, T., and Fesik, S. W. (1996) *Biochemistry 35*, 2095−2103.
66. Kay, L. E., Torchia, D. A., and Bax, A. (1989) *Biochemistry 28*, 8972−8979.
67. Englander, S. W., and Kallenbach, N. R. (1984) *Q. Rev. Biophys. 16*, 521−655.
68. Bai, Y., Milne, J. S., Mayne, L., and Englander, S. W. (1993) *Proteins 17*, 75−86.
69. Gronenborn, A. M., and Clore, G. M. (1994) *J. Biomol. NMR 4*, 455−458.
70. Gryk, M. R., Finucane, M. D., Zheng, Z., and Jardetzky, O. (1995) *J. Mol. Biol. 246*, 618−627.
71. Weiss, M. A., Ellenberger, T., Wobbe, C. R., Lee, J. P., Harrison, S. C., and Struhl, K. (1990) *Nature 347*, 575−578.
72. Liang, H., Olejniczak, E. T., Mao, X. H., Nettesheim, D. G., Yu, L. P., Thompson, C. B., and Fesik, S. W. (1994) *Proc. Natl. Acad. Sci. U.S.A. 91*, 11655−11659.
73. Lewis, H. A., Musunuru, K., Jensen, K. B., Edo, C., Chen, H., Darnell, R. B., and Burley, S. K. (2000) *Cell 100*, 323−332.
74. Garrett, D. S., Seok, Y. J., Peterkofsky, A., Clore, G. M., and Gronenborn, A. M. (1997) *Biochemistry 36*, 4393−4398.

BI000105E